

# Fabrication and characterization of vacuum-gap microstrip resonators

Christian Schlager,<sup>1,2</sup> Romain Albert,<sup>1,2,3</sup> and Gerhard Kirchmair<sup>1,2</sup>

<sup>1)University of Innsbruck, Institute for Experimental Physics, Innsbruck, Austria</sup>

<sup>2)Institute for Quantum Optics and Quantum Information,  
Austrian Academy of Sciences, Innsbruck, Austria</sup>

<sup>3)Current Address: Silent Waves, 69-73 rue Félix Esclangon, 38000 Grenoble, France</sup>

(christian.schlager@uibk.ac.at)

In traveling-wave parametric amplifiers (TWPAs) low-loss capacitors are necessary to provide  $50\ \Omega$  impedance matching to the increased inductance that is brought in by the nonlinear elements used for amplification, be it Josephson junctions or high kinetic inductance materials. Here we report on the development of a fabrication process for vacuum-gap microstrips, a design in which the ground plane is suspended in close proximity above the center conductor without the support of a dielectric. In addition to high-capacitance transmission lines, this architecture also enables air-bridges and compact parallel-plate capacitors. The performance of the fabrication is examined using distributed aluminum and granular aluminum resonators in a cryogenic dilution refrigerator setup, showing quality factors on par with the fabrication processes used in state-of-the-art TWPAs. In addition to characterizing the dependence of the quality factors on power, also their behavior with respect to temperature is explored, applying a model based on thermal quasi-particles and saturable two-level systems (TLS), showing that the quality factors of the resonators are limited by TLS.

Implementing low-footprint capacitance while simultaneously keeping dielectric losses low is a challenge in fabricating superconducting resonators<sup>1</sup> and circuits in general. Especially traveling-wave parametric amplifiers (TWPAs) using Josephson junctions or high kinetic inductance materials have a need for large, compact and low-loss capacitors to achieve impedance matching, which is necessary for preventing unwanted reflections<sup>2</sup>.

While the first implementations of TWPAs<sup>3,4</sup> made use of impedance transformers on both ends of the amplifier, state-of-the-art designs either use interdigitated coplanar capacitors<sup>5,6</sup> or parallel-plate like geometries with a dielectric layer in between<sup>7-13</sup> to achieve  $50\ \Omega$  matching. Coplanar designs are usually lower in loss, due to the lower participation of surfaces, interfaces and non-crystalline dielectrics. Achieving large capacitance in this geometry however requires large-footprint structures and dedicated addressing of the ground plane. Parallel-plate capacitors offer large capacitance with compact footprint and an uninterrupted ground plane. However, TWA devices using this design are often suspected to be limited in their noise performance by the dielectric loss introduced by the amorphous dielectrics in the capacitors. Realizing a microstrip with a vacuum-gap instead of the conventional lossy dielectric layer between the two conductors is therefore a promising approach for realizing compact capacitors while maintaining comparably low losses.

Vacuum-gap air-bridges are frequently used to bridge over planar structures and ensure ground plane connectivity over a chip divided by coplanar waveguides<sup>14-17</sup>. However, they are usually designed with heights of micrometers to not significantly alter the impedance of the transmission line they are spanning. To significantly increase the capacitance of the transmission line, the vacuum-gap structure has to be suspended at distances of tens to hundreds of nanometers. This has been done using sacrificial layers of Si, Nb or  $\text{SiN}_x$ <sup>18,19</sup> or Al<sup>20</sup>. In these cases, the process for removing the sacrificial layer limits the potential materials the process can be combined with.

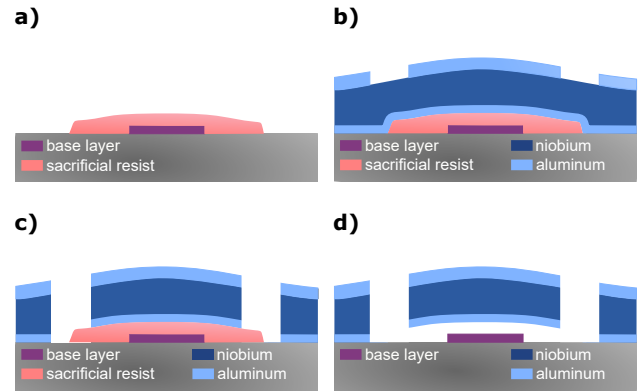


FIG. 1. Schematic depiction of the fabrication process. (a) An 80 nm thick layer of resist covers the base layer, protecting it and acting as a sacrificial placeholder. (b) The triple-layer ground plane is deposited on top with holes patterned in the topmost aluminum layer. (c) The aluminum mask enables the etching of access holes down to the sacrificial resist. (d) Through the holes the sacrificial resist is removed by organic solvents before the vacuum-gap microstrip is released by critical-point drying. Dimensions in horizontal and vertical direction are not to scale. Typical widths of the sacrificial resist used for the samples in this work are around  $10\ \mu\text{m}$ , while the thickness of the sacrificial resist is 80 nm.

The fabrication process described in this work uses a thin film of resist as a sacrificial layer that is afterwards removed by organic solvents to create a vacuum-gap (VG) microstrip. This increases the compatibility to a wide range of different materials within the same design. We have fabricated aluminum and granular aluminum (grAl) resonators coupled to the same transmission line, assessed their quality factors and also explored their behavior with temperature.

The first step of the fabrication process is the definition of the base layer on a silicon substrate (see fig 1 (a)). In the resonator samples fabricated, the base layer contains sputtered granular aluminum<sup>21</sup> (grAl) and evaporated aluminum, pat-

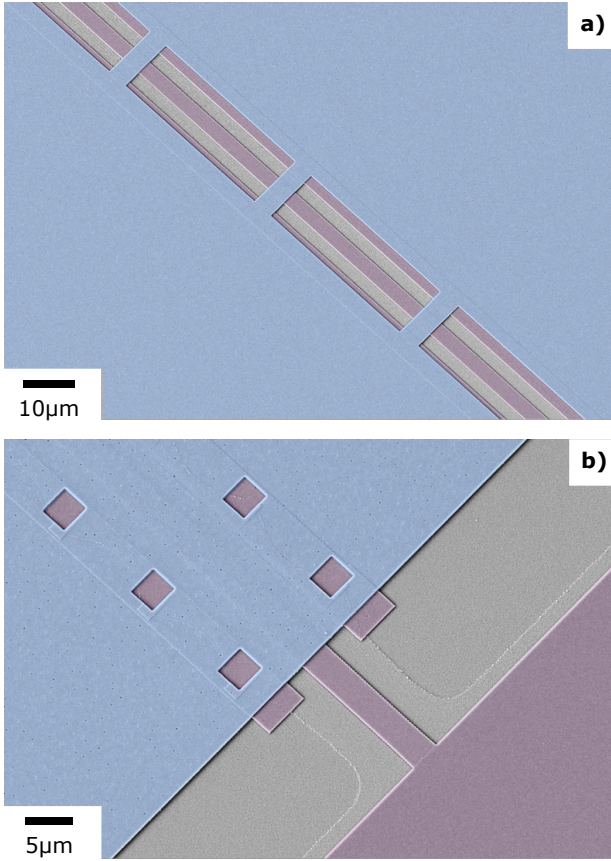


FIG. 2. SEM false color images of different vacuum-gap microstrip structures. Analogous to figure 1, purple indicates the base layer, blue the ground plane and gray the substrate. (a) VG air-bridges over a CPW transmission line. (b) VG-microstrip with access holes through the ground plane starting from a bonding pad (lower right corner). The two strips parallel to the center conductor enhance the adhesion of the sacrificial resist to the substrate. The dark spots that can be seen on the ground plane are due to superficial damage done to the outermost aluminum layer by the last etching step. In both images the sacrificial resist has been removed, the outline of where it was can be seen in (b) where the silicon surface was partly protected by the resist during the last etching step.

terned and deposited in subsequent steps. First the granular aluminum is deposited by sputtering in an Ar + O<sub>2</sub> atmosphere (see appendix A). We choose a kinetic inductance of approximately 100 pH/□. The aluminum is deposited afterwards in a separate lift-off process. As a spacer for the future vacuum-gap, the wafer is coated with an 80 nm thick sacrificial layer of the negative resist ma-N 2401, which is patterned using electron-beam lithography (see fig. 1 (a)). The resist is overdosed to obtain rounded edges. To guarantee sufficient adhesion of the sacrificial resist as well as a well-defined gap between center conductor and ground-plane, additional metal strips in the base layer are used (visible in fig. 2 (b)). The metasilicate-based developer ma-D 377 is used instead of TMAH-based alternatives to ensure compatibility with aluminum.

TABLE I. Loss comparison of our approach to successful implementations of TWPAs in parallel-plate geometry.

publication	dielectric	tan $\delta$
Shan et al. <sup>8,23</sup>	50 nm SiO <sub>2</sub>	$5 \times 10^{-4}$
Planat et al. <sup>10-12,24</sup>	30 nm Al <sub>2</sub> O <sub>3</sub>	$6.5 \times 10^{-3}$
Shu et al. <sup>9,25</sup>	200 nm aSi:H	$3.6 \times 10^{-5}$
this work	80 nm vacuum	$3 \times 10^{-4}$

The patterned sacrificial resist is covered by a double layer ground plane consisting of an inner layer of evaporated aluminum (10 nm thick) and the strain-free sputtered niobium main body (300 nm thick), deposited in a combined evaporation and sputtering process without breaking vacuum in between. To ensure electrical contact to the base layer, the aluminum evaporation is preceded by Ar ion milling to remove any native oxides. Finally, a patterned layer of aluminum is deposited through a lift-off process (see fig. 1 (b)).

The niobium layer of the ground plane is etched using CF<sub>4</sub> + O<sub>2</sub> reactive ion etching (RIE). This chemistry is highly selective between the aluminum mask and the niobium main layer. The etching stops at the innermost thin layer of aluminum, preventing any risk of etching into the sacrificial resist and potentially harming the base layer. Finally the inner layer of the ground plane is etched in the same RIE using a combined BCl<sub>3</sub> and Ar plasma (see fig. 1 (c)).

We deploy a sequence of organic solvents (N-Methyl-2-pyrrolidone (NMP), acetone and ethanol) to remove the sacrificial resist and release the ground plane (see fig. 1 (d)). To ensure optimal removal of the sacrificial resist the sample is left for two days in NMP, one day in acetone and one day in ethanol. Without letting the wafer dry at any point during this process, it is transferred in ethanol to a critical point dryer to release the ground plane without collapsing the structure due to surface tension, similar to MEMS fabrication processes<sup>22</sup>.

To examine the microwave performance of the presented fabrication process, resonators were fabricated in hanger configuration along a transmission line. The transmission line is implemented as a coplanar waveguide with air-bridges every 50  $\mu\text{m}$  for good electrical connection of the ground plane (see fig. 2 (a)). This transmission line is coupled to multiple  $\lambda/4$  resonators in vacuum-gap architecture with center conductors made of two different materials, aluminum and granular aluminum. The coupling is done with parallel-plate vacuum-gap capacitive couplers. The samples are wire-bonded to a PCB in a copper sample holder and placed inside a dilution refrigerator. At base-temperature the transmission of the lines is probed using a vector network analyzer. The quality factors of a total of 21 resonators were extracted by performing circle fits<sup>26-28</sup> to the transmission data through the feedline and are shown in fig. 3. The x-axis shows the average number of photons  $\bar{n}$ , populating the resonator on resonance. It is calculated from the internal and coupling quality factors and the incident power  $P_{\text{inc}}$  at the sample via<sup>29</sup>

$$\bar{n} = \frac{2Q_l^2}{Q_c \hbar \omega^2} P_{\text{inc}}, \quad (1)$$

where  $Q_l$  denotes the loaded and  $Q_c$  the coupling quality fac-

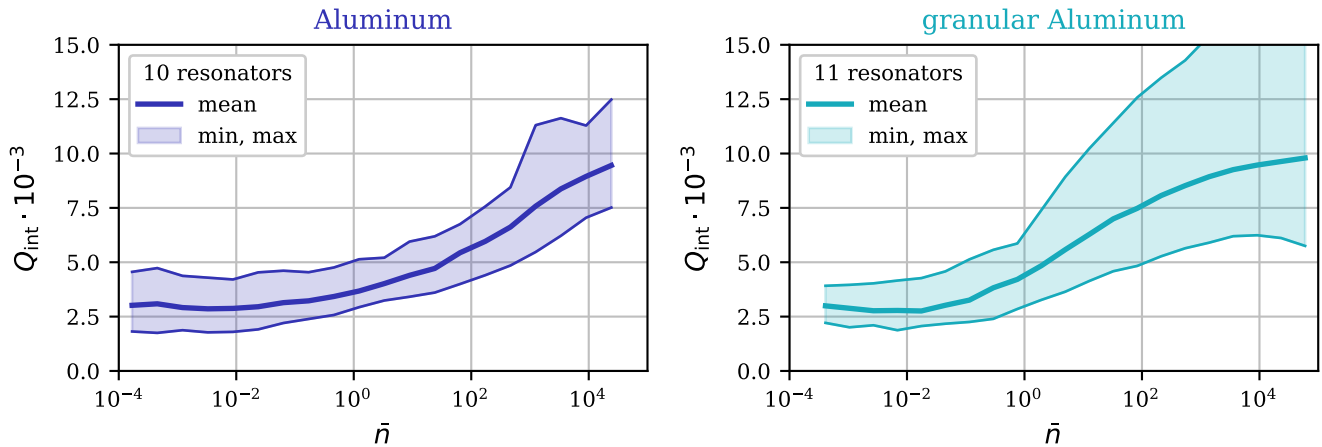


FIG. 3. Internal quality factors of aluminum (**left**) and granular aluminum (**right**) vacuum-gap microstrip resonators over average photon number  $\bar{n}$  as obtained from circle fits to VNA transmission data. The data of all resonators is contained within the shaded regions, while the line in the center represents the average. For the raw data of the individual resonators see appendix B.

tor of the resonator,  $\omega$  is the angular resonance frequency. The incident power at the sample is obtained by determining the output gain of the measurement chain via a Y-factor measurement<sup>30</sup> using two thermalized  $50\ \Omega$  loads at 20 mK and 4 K respectively. With increasing power, i.e. higher average photon number in the resonator, we see an increase in the internal quality factors due to saturation of losses connected to two level systems (TLS).

The quality factors for low powers can be seen towards the left part of the diagrams in fig. 3, where the curves flatten out. For the noise added to a small signal propagating through an amplifier, the low power loss of the device is essential. The losses for high powers are important for the attenuation suffered by a strong pump tone or the amplified signal propagating through the system, thus limiting the gain. From the low-power section of fig. 3 we read quality factors of  $Q_{\text{int}} \approx 3000$ , or loss tangents of  $\tan \delta \approx 3 \times 10^{-4}$  respectively.

It has to be noted, that previous works on vacuum-gaps, using Si, Nb or  $\text{SiN}_x$ <sup>18,19</sup> or Al<sup>20</sup> as a sacrificial layer, have seen higher quality factors for their capacitors of  $Q_{\text{int}} = 2.5$  to  $3.3 \times 10^4$  or  $Q_{\text{int}} = 4.3 \times 10^5$  respectively. We mainly attribute the excessive loss of our device to resist residues that remain in the VG-microstrips. Also it is worth noting that the vacuum-gap in this work is by a factor of 2 to 4 smaller than the other approaches mentioned, leading to an increased participation of the involved surfaces. Comparing the VG-microstrip resonators to successful implementations of traveling-wave parametric amplifiers, however, shows that the achieved quality factors are indeed sufficient for this application and do in fact compare favorably (see tab.I). As dielectric loss is one of the main suspects for noise exceeding the quantum limit in TWPAs<sup>2</sup>, we conclude that the fabrication method presented here is a promising candidate for their implementation.

To further investigate the origin of the losses of the resonators as well as to gain insight into the material properties of the aluminum and granular aluminum used as their center conductor, the fridge temperature is swept progressively in

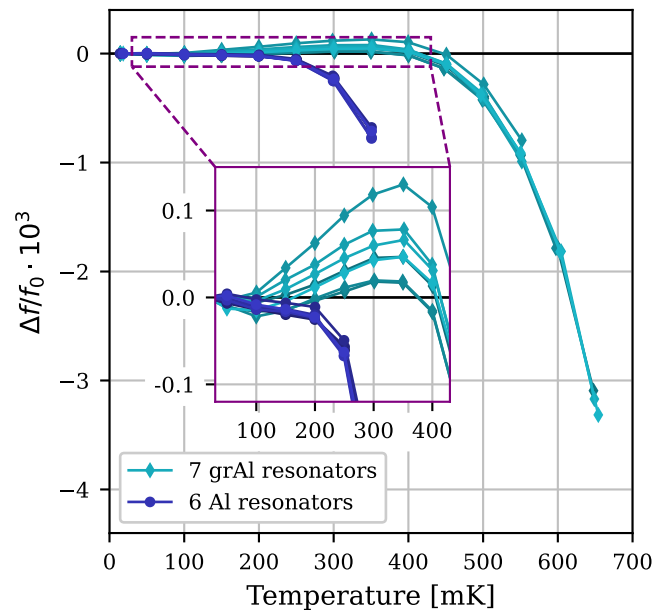


FIG. 4. Relative change in resonance frequency over temperature. Turquoise diamond markers resemble resonators made from granular aluminum, blue circles mark those made from pure aluminum. The inset shows a zoom in on the region between 30 mK and 430 mK. The lines connecting the markers are guides for the eye.

steps of 50 mK up to 700 mK. Beyond this temperature none of the resonances can be fitted reliably anymore. With increasing temperature we observe a decrease in internal quality factors as well as shifts in resonance frequency for all resonators. The corresponding data is shown in fig. 4. The temperature at which the resonance frequency starts to drop differs for aluminum and grAl resonators. The shift to lower frequencies for higher temperatures as well as the increase in frequency in

the range 100 mK to 400 mK shown by the granular aluminum resonators can be explained by a combination of coupling to

TLS in the dielectric and thermal quasi-particles according to the Mattis-Bardeen model<sup>29,31–33</sup>:

$$\frac{f(T) - f_0}{f_0} = \frac{F \tan \delta}{\pi} \left( \operatorname{Re} \left[ \Psi \left( \frac{1}{2} + \frac{hf}{2i\pi k_B T} \right) \right] - \log \left( \frac{hf}{2\pi k_B T} \right) \right) - \frac{\alpha}{2} \sqrt{\frac{\pi \Delta_{S0}}{2k_B T}} \exp \left( \frac{-\Delta_{S0}}{k_B T} \right). \quad (2)$$

Here  $F \tan \delta$  is the loss tangent of the material connected to the TLS combined with its filling factor  $F$  and  $\Psi$  is the complex digamma function. The kinetic inductance fraction  $\alpha = L_{\text{kin}}/L_{\text{tot}}$  is the fraction of the kinetic inductance  $L_{\text{kin}}$  of the resonator over the total inductance  $L_{\text{tot}}$ , which is the sum of the kinetic and geometric inductance.  $\Delta_{S0}$  denotes the superconducting energy gap at zero temperature. It is worth noting, that the effect of the TLS is more noticeable in the granular aluminum resonators but also manifests in the aluminum resonators (see appendix B). The more pronounced effect in the granular aluminum is due to two reasons. Firstly the larger superconducting gap forces the frequency down at comparably higher temperature, revealing more of the TLS effect in the temperature range of 150 mK to 400 mK. As a second factor, it has to be mentioned that by design, the granular aluminum resonators reside in a lower frequency range than the aluminum resonators, namely  $4 \text{ GHz} < f_{\text{grAl}} < 6.5 \text{ GHz}$ , compared to  $7.5 \text{ GHz} < f_{\text{Al}} < 10 \text{ GHz}$ .

Using eq. 2, we can extract  $\Delta_{S0}$  and  $F \tan \delta$  by fitting it to the data presented in fig. 4. To obtain reliable fits, either the kinetic inductance fraction  $\alpha$  or the superconducting gap  $\Delta_{S0}$ , has to be fixed. For the granular aluminum  $\alpha = 0.999(1)$  is very close to unity because of the large kinetic inductance and hence also the uncertainty introduced by the exact value of the geometric inductance vanishes. The fitting results can be seen in tab. II. We obtain a superconducting gap of  $\Delta_{S0} = 351(2) \mu\text{eV}$  and a loss tangent of  $F \tan \delta = 5.9(14) \times 10^{-4}$ . The values in brackets resemble the empirical standard deviation of the fit results of the individual data sets (cf. appendix C). The value for the superconducting gap and the resulting critical temperature  $T_c = 2\Delta_{S0}/(3.53k_B) = 2.31(2) \text{ K}$  that we obtain for the granular aluminum lie within the range of values reported in the literature<sup>21,34,35</sup>. For the aluminum resonators, however, the kinetic inductance is expected to neither dominate, nor vanish compared to the geometric inductance of the resonator. This is because of the geometric inductance  $L_{\text{geom}}$  being suppressed by the close proximity of the suspended ground plane. Assuming the width  $w$  of the center conductor being much larger than the vacuum-gap  $h$ , we arrive at the approximate formula (see appendix D):

$$L_{\text{geom}} = \mu_0 \frac{h}{w}. \quad (3)$$

Consequently for the aluminum resonators we fix the superconducting gap and fit the data with the resulting function. From trying different fits we can conclude, that only a superconducting gap in the range  $\Delta_{S0} = 190 \mu\text{eV}$  to  $230 \mu\text{eV}$  agrees with the observed data (see appendix C). A value of

TABLE II. Parameters extracted by fitting eq. 2 to the data from fig. 4. For the granular aluminum resonators the uncertainty given resembles the empirical standard deviation of the fits to the individual datasets. In contrast, for the aluminum, multiple different values were set for the superconducting gap  $\Delta_{S0}$  and the resulting spread in the respective best fitting parameters is given.

	granular aluminum	aluminum
number of resonators	7	6
fixed parameters	$\alpha = 0.999$	$\Delta_{S0} = 210(20) \mu\text{eV}$
fitted parameters	$F \tan \delta = 5.9(14) \times 10^{-4}$ $\Delta_{S0} = 351(2) \mu\text{eV}$	$F \tan \delta = 2.5(10) \times 10^{-4}$ $\alpha = 0.6(3)$

$210(20) \mu\text{eV}$  is consistent with the literature<sup>36</sup> and also leads to a kinetic inductance fraction  $\alpha = 0.6(3)$  consistent with our expectations from finite element electromagnetic simulations.

To conclude, we have developed a fabrication process for vacuum-gap microstrips and demonstrated their performance by implementing distributed  $\lambda/4$  resonators. The fabrication process enables air-bridges, compact lumped-element capacitors and high capacitance transmission lines. The achieved quality factors compare favorably to parallel plate designs using a dielectric to separate the ground plane from the base layer. The grAl and aluminum samples were also investigated for their behavior with temperature. The different critical temperatures of the two materials could be observed as well as the influence of TLS, which limit the quality factors of the fabricated resonators.

This process is very promising for the fabrication of quantum-limited TWPAs. Only using low temperature steps and no aggressive chemicals, it is in principle compatible with almost all materials, notably including Josephson junctions as well as high-kinetic inductance materials. Therefore, the process is also compatible with the integration of superconducting qubits and low speed of light transmission lines, possibly facilitating multiple qubit entanglement in a compact system. Finally, it makes it possible to realize compact on-chip capacitors and strong capacitive couplers which are useful for the implementation of microwave detectors.

## ACKNOWLEDGMENTS

This project has received funding from the Horizon Europe 2021-2027 project TruePA of the European Union (grant agreement number 101080152). RA was funded in part by



the Austrian Science Fund (FWF) DOI 10.55776/F71. For the purpose of open access, the authors have applied a CC BY public copyright license to any Author Accepted Manuscript version arising from this submission.

- <sup>1</sup>J. Zmuidzinas, Annual Review of Condensed Matter Physics **3**, 169 (2012).
- <sup>2</sup>M. Esposito, A. Ranadive, L. Planat, and N. Roch, Applied Physics Letters **119**, 120501 (2021).
- <sup>3</sup>B. Ho Eom, P. K. Day, H. G. LeDuc, and J. Zmuidzinas, Nature Physics **8**, 623 (2012).
- <sup>4</sup>C. Bockstiegel, J. Gao, M. R. Vissers, M. Sandberg, S. Chaudhuri, A. Sanders, L. R. Vale, K. D. Irwin, and D. P. Pappas, Journal of Low Temperature Physics **176**, 476 (2014).
- <sup>5</sup>A. A. Adamyan, S. E. de Graaf, S. E. Kubatkin, and A. V. Danilov, Journal of Applied Physics **119**, 083901 (2016).
- <sup>6</sup>M. Malnou, M. Vissers, J. Wheeler, J. Aumentado, J. Hubmayr, J. Ullom, and J. Gao, PRX Quantum **2**, 010302 (2021).
- <sup>7</sup>C. Macklin, K. O'Brien, D. Hover, M. E. Schwartz, V. Bolkhovskiy, X. Zhang, W. D. Oliver, and I. Siddiqi, Science **350**, 307 (2015).
- <sup>8</sup>W. Shan, Y. Sekimoto, and T. Noguchi, IEEE Transactions on Applied Superconductivity **26**, 1 (2016).
- <sup>9</sup>N. Klimovich, P. Day, S. Shu, B. H. Eom, H. Leduc, and A. Beyer, "Demonstration of a Quantum Noise Limited Traveling-Wave Parametric Amplifier," (2023), arXiv:2306.11028.
- <sup>10</sup>A. Ranadive, B. Fazlji, G. L. Gal, G. Cappelli, G. Butseraen, E. Bonet, E. Eyraud, S. Böhring, L. Planat, A. Metelmann, and N. Roch, "A Traveling Wave Parametric Amplifier Isolator," (2024), arXiv:2406.19752.
- <sup>11</sup>A. Ranadive, M. Esposito, L. Planat, E. Bonet, C. Naud, O. Buisson, W. Guichard, and N. Roch, Nature Communications **13**, 1737 (2022).
- <sup>12</sup>L. Planat, A. Ranadive, R. Dassonneville, J. Puertas Martínez, S. Léger, C. Naud, O. Buisson, W. Hasch-Guichard, D. M. Basko, and N. Roch, Physical Review X **10**, 021021 (2020).
- <sup>13</sup>A. Fadavi Roudsari, D. Shiri, H. Renberg Nilsson, G. Tancredi, A. Osman, I.-M. Svensson, M. Kudra, M. Rommel, J. Bylander, V. Shumeiko, and P. Delsing, Applied Physics Letters **122**, 052601 (2023).
- <sup>14</sup>M. Abuwasib, P. Krantz, and P. Delsing, Journal of Vacuum Science & Technology B Microelectronics and Nanometer Structures **31**, 031601 (2013).
- <sup>15</sup>Z. Chen, A. Megrant, J. Kelly, R. Barends, J. Bochmann, Y. Chen, B. Chiaro, A. Dunsworth, E. Jeffrey, J. Y. Mutus, P. J. J. O'Malley, C. Neill, P. Roushan, D. Sank, A. Vainsencher, J. Wenner, T. C. White, A. N. Cleland, and J. M. Martinis, Applied Physics Letters **104**, 052602 (2014).
- <sup>16</sup>N. Janzen, M. Kononenko, S. Ren, and A. Lupascu, Applied Physics Letters **121**, 094001 (2022).
- <sup>17</sup>Z.-C. Jin, H.-T. Wu, H.-F. Yu, and Y. Yu, Chinese Physics B **27**, 100310 (2018).
- <sup>18</sup>K. Cicak, M. S. Allman, J. A. Strong, K. D. Osborn, and R. W. Simmonds, IEEE Transactions on Applied Superconductivity **19**, 948 (2009).
- <sup>19</sup>K. Cicak, D. Li, J. A. Strong, M. S. Allman, F. Altomare, A. J. Sirois, J. D. Whittaker, J. D. Teufel, and R. W. Simmonds, Applied Physics Letters **96**, 093502 (2010).
- <sup>20</sup>F. Boussaha, S. Beldi, A. Monfardini, J. Hu, M. Calvo, C. Chaumont, F. Levy-Bertrand, T. Vacelet, A. Traini, J. Firminy, M. Piat, and F. Reix, Journal of Low Temperature Physics **199**, 994 (2020).
- <sup>21</sup>H. Rotzinger, S. T. Skacel, M. Pfirrmann, J. N. Voss, J. Münzberg, S. Probst, P. Bushev, M. P. Weides, A. V. Ustinov, and J. E. Mooij, Superconductor Science and Technology **30**, 025002 (2017).
- <sup>22</sup>I. H. Jafri, H. Busta, and S. T. Walsh, in *MEMS Reliability for Critical and Space Applications*, Vol. 3880 (SPIE, 1999) pp. 51–58.
- <sup>23</sup>W. Shan, Y. Sekimoto, and T. Noguchi, Japanese Journal of Applied Physics **54**, 090303 (2015).
- <sup>24</sup>L. Planat, E. Al-Tavil, J. P. Martínez, R. Dassonneville, F. Foroughi, S. Léger, K. Bharadwaj, J. Delaforce, V. Milchakov, C. Naud, O. Buisson, W. Hasch-Guichard, and N. Roch, Physical Review Applied **12**, 064017 (2019).
- <sup>25</sup>S. Shu, N. Klimovich, B. H. Eom, A. D. Beyer, R. B. Thakur, H. G. Leduc, and P. K. Day, Physical Review Research **3**, 023184 (2021).
- <sup>26</sup>S. Probst, F. B. Song, P. A. Bushev, A. V. Ustinov, and M. Weides, Review of Scientific Instruments **86**, 024706 (2015).
- <sup>27</sup>J. Gao, *The physics of superconducting microwave resonators*, Ph.D. thesis, California Institute of Technology (2008).
- <sup>28</sup>C. Deng, M. Otto, and A. Lupascu, Journal of Applied Physics **114**, 054504 (2013).
- <sup>29</sup>A. Bruno, G. de Lange, S. Asaad, K. L. van der Enden, N. K. Langford, and L. DiCarlo, Applied Physics Letters **106**, 182601 (2015).
- <sup>30</sup>D. M. Pozar, *Microwave engineering*, 4th ed. (Wiley, Hoboken, NJ, 2012).
- <sup>31</sup>D. Pappas, M. Vissers, D. Wisbey, J. Kline, and J. Gao, Applied Superconductivity, IEEE Transactions on **21**, 871 (2011).
- <sup>32</sup>T. Tai, J. Cai, and S. M. Anlage, Advanced Quantum Technologies **7**, 2200145 (2024).
- <sup>33</sup>L. Grünhaupt, N. Maleeva, S. T. Skacel, M. Calvo, F. Levy-Bertrand, A. V. Ustinov, H. Rotzinger, A. Monfardini, G. Catelani, and I. M. Pop, Physical Review Letters **121**, 117001 (2018).
- <sup>34</sup>F. Levy-Bertrand, T. Klein, T. Grenet, O. Dupré, A. Benoît, A. Bideaud, O. Bourrion, M. Calvo, A. Catalano, A. Gomez, J. Goupy, L. Grünhaupt, U. v. Luepke, N. Maleeva, F. Valenti, I. M. Pop, and A. Monfardini, Physical Review B **99**, 094506 (2019).
- <sup>35</sup>U. S. Pracht, N. Bachar, L. Benfatto, G. Deutscher, E. Farber, M. Dressel, and M. Scheffler, Physical Review B **93**, 100503 (2016).
- <sup>36</sup>N. Court, A. Ferguson, and R. Clark, Superconductor Science and Technology **21**, 015013 (2007).

## Appendix A: Granular aluminum sputtering

The granular aluminum used as the central conductor for the resonators in this work was deposited by DC sputtering of an aluminum target in an Ar + O<sub>2</sub> atmosphere. The gas flow into the chamber is controlled by two mass flow controllers, one dispensing pure Ar gas, while the other one controls the flow of a 95 % Ar and 5 % O<sub>2</sub> gas mixture. This setup enables finer control and more stable application of the oxygen compared to the use of pure oxygen. Fine tuning of oxygen abundance, sputtering power as well as annealing temperature after the process facilitates control over the normal state resistance and thereby the kinetic inductance of the deposited film. Also it was found that flooding of the chamber with oxygen before the sputter deposition leads to enhanced reproducibility of the process.

## Appendix B: Quality factors

The data used for the assessment of the quality factors of the VG-microstrips as it is presented in fig. 3 stems from resonators distributed over three transmission lines in two cool-downs. All data used to produce the plots can be seen in fig. 5. Of the 12 granular aluminum resonators that were cooled down, 11 could be observed. For the aluminum resonators this number is 10 out of 15, with some of them likely falling out of the measurement band. To generate the plots in the main text, combining all the data into a compact depiction using the average as well as the minimum and maximum, the data is organized in bins. These bins are equally spaced and their number (21 for the grAl and 20 for the aluminum resonators) was chosen to avoid artifacts of this method, such as fluctuations in the average curve due to sampling.

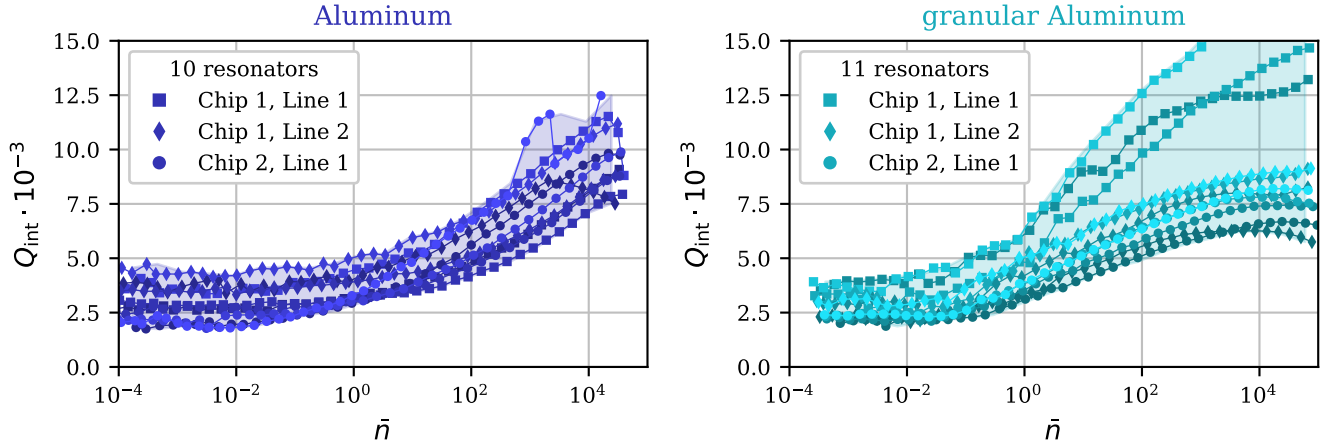


FIG. 5. Internal quality factors of aluminum (**left**) and granular aluminum (**right**) vacuum-gap microstrip resonators over average photon number  $\bar{n}$  as obtained from circle fits to VNA transmission data. The lines between data points serve as guides to the eye.

### Appendix C: Temperature dependence

In order to investigate the temperature dependence of the resonators, the base temperature of the dilution refrigerator is swept up to 1 K in the cool-down containing "Chip 1". The data of all resonators used to produce fig. 4 is shown in fig. 6 together with the fits mentioned in the main text. The curves are shown with artificial offsets, to improve visibility.

As the kinetic inductance fraction  $\alpha$  is not well known for the aluminum, the superconducting gap  $\Delta_{S0}$  has to be fixed for the fit. Trying different plausible values for  $\Delta_{S0}$ , we arrive at the conclusion, that the behavior of the data in the region between 100 mK to 250 mK is best captured by  $\Delta_{S0} = 210 \mu\text{eV}$ , but an uncertainty on that value of  $\pm 20 \mu\text{eV}$  is estimated. This uncertainty consequently leads to a spread in the extracted fit parameters. As this spread is larger than the empirical standard deviation of the collection of data sets, it is therefore given as the error on the fit results. To further investigate the material parameters of the aluminum used for the center conductor of the resonators, the critical temperature of the specific thin-film as well as more dense data especially in the region 100 mK to 250 mK would be required, which was not the focus of this study. Also, resonators at a lower resonant frequency would show more a pronounced TLS effect.

In contrast to the aluminum resonators, the resonators made from grAl are heavily dominated by kinetic inductance due to the (100 pH/ $\square$ ) kinetic inductance of the film and the suppressed geometric inductance stemming from the microstrip geometry (see D). This allows us to fix it to 99.9(1) % with much larger accuracy compared to the aluminum resonators. Consequently the empirical standard deviation between fitting parameters of different resonators is given as the error on the respective values.

### Appendix D: Inductance of a microstrip

To estimate the geometric inductance  $L_{\text{geom}}$  of the VG-microstrips we consider two parallel conducting plates with length  $l$  separated by a distance  $h$ . The width  $w$  of the bottom plate is less than that of the top ground plane. In the following we will assume  $l \gg w \gg h$ . The two plates carry two currents  $I$ , equal and opposite in direction along the  $z$ -axis, for which we assume a homogeneous distribution along the plate in the region where the two plates overlap (see fig. 7). The resulting magnetic field is constant in the space between the plates. Applying Ampère's law to loops around the two plates individually, we obtain:

$$\oint_{S_1} \vec{B} d\vec{s} = w(-B_2 + B_1) = \mu_0 I \quad (\text{D1})$$

$$\oint_{S_2} \vec{B} d\vec{s} = w(B_3 - B_2) = \mu_0 I \quad (\text{D2})$$

Note that the direction of integration around the plates has been chosen in such a way to match the direction of the current in the respective conductor. Due to the distance between the plates being much smaller than their width, the homogeneous fields created by the two current sheets cancel outside the arrangement, i.e.  $B_1 = B_3 = 0$ . Therefore from equations D1 and D2 we obtain:

$$B_2 = -\frac{\mu_0 I}{w}, \quad (\text{D3})$$

meaning a  $\vec{B}$ -field in negative  $x$ -direction and with absolute value  $|\vec{B}| = \mu_0 I/w$ . To find the inductance  $L = \Phi_m/I$ , we first find the magnetic flux  $\Phi_m$  through a one unit length long cross section of the center space between the two plates

$$\Phi_m = \int_0^1 \int_0^h \frac{\mu_0 I}{w} dy dz = \frac{\mu_0 h I}{w}. \quad (\text{D4})$$

This directly yields the inductance per unit length:

$$L_{\text{geom}} = \mu_0 \frac{h}{w}. \quad (\text{D5})$$

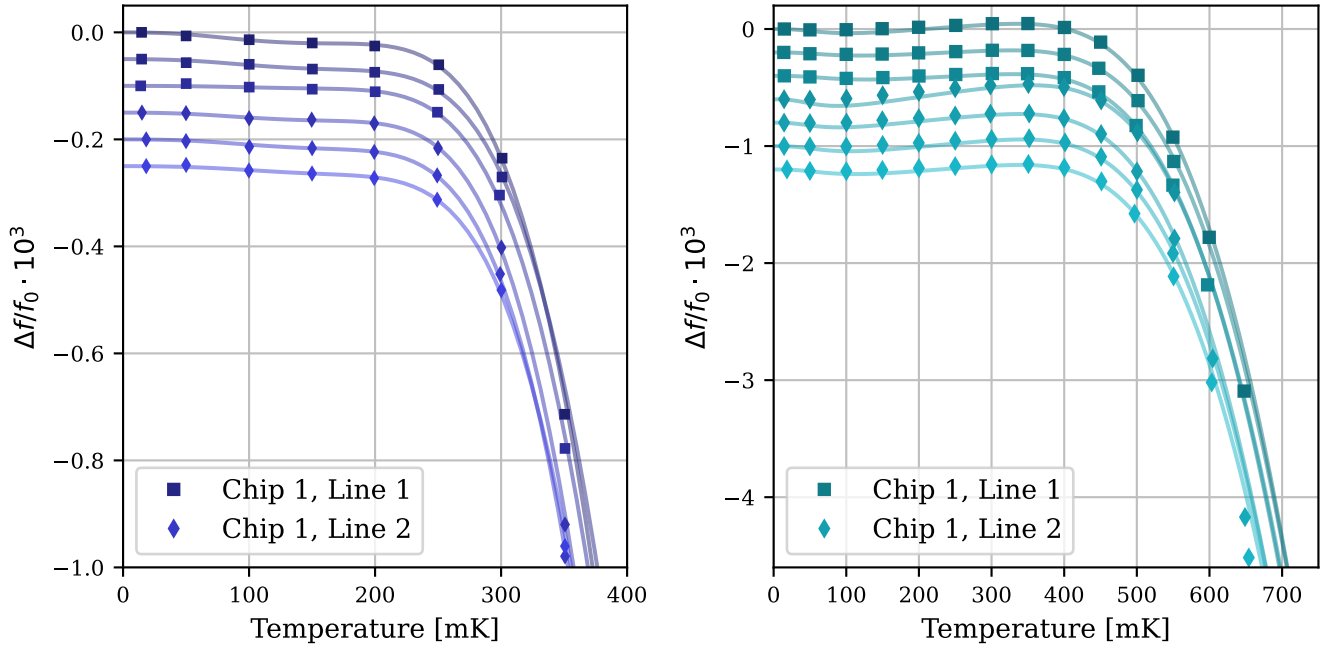


FIG. 6. Relative change in resonance frequency over temperature with best fits to eq. 2. The data and fits of different resonators are artificially offset for better visibility. **(left:)** To fit the aluminum resonators, the superconducting gap was fixed. The fits shown here are for  $\Delta_{S0} = 210 \mu\text{eV}$ , but an uncertainty of  $\pm 20 \mu\text{eV}$  is estimated. **(right:)** For the granular Aluminum resonator, the kinetic inductance fraction is fixed to  $\alpha = 0.999$ .

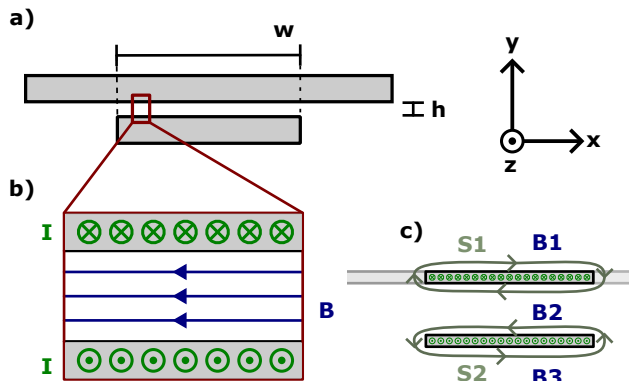


FIG. 7. Sketch illustrating the calculation of the geometric inductance of a conductor in microstrip geometry.

The geometric factor  $h/w$  makes clear how the geometry of the VG-microstrip is able to suppress the geometric inductance. If we plug in typical numbers for our resonators, we arrive at

$$L_{\text{geom}} \approx 1.257 \times 10^{-6} \text{ N/A}^2 \times \frac{80 \text{ nm}}{4 \mu\text{m}} \approx 25 \text{ nH/m}. \quad (\text{D6})$$

This value agrees with the results of our finite element simulations within 6%. We attribute the remaining discrepancy mostly to the assumptions taken in this analytical approach, namely possible fringe effects at the edges of the smaller one of the conducting sheets.